

1 **PM_{2.5} Assimilation within JEDI for NOAA's Regional Air**

2 **Quality Model (AQMv7): Application to the September 2020**

3 **Western U.S. Wildfires**

4

5 Hongli Wang^{1,2}, Cory Martin³, Jérôme Barré^{4,5}, Ruifang Li^{1,2}, Steve Weygandt², Jianping Huang³,

6 Youhua Tang^{6,7}, Hyundeok Choi^{8,3}, Andrew Tangborn^{8,3}, Kai Wang^{9,3}, Haixia Liu^{9,3}, Jeffrey Lee¹⁰

7

8 1. Cooperative Institute for Research In Environmental Sciences, University of Colorado, Boulder, CO 80305

9 2. NOAA Global Systems Laboratory, Boulder, CO 80305

10 3. NOAA/NWS/NCEP/EMC, College Park, MD 20740

11 4. NASA Global Modeling and Assimilation Office, Greenbelt, MD, USA

12 5. Morgan State University, Baltimore, MD, USA

13 6. Center for Spatial Information Science and Systems, George Mason University, Fairfax, VA 22030

14 7. NOAA Air Resources Laboratory (ARL), College Park, MD 20740

15 8. SAIC@NOAA/NWS/NCEP/EMC, College Park, MD 20740

16 9. LINKER@NOAA/NWS/NCEP/EMC, College Park, MD 20740

17 10. School of Meteorology, University of Oklahoma, Norman, OK 73072

18 *Correspondence to:* Hongli Wang (hongli.wang@noaa.gov)

19 **Abstract.** This paper describes efforts to establish aerosol data assimilation capabilities for NOAA's National Air
20 Quality Forecasting Capability (NAQFC), a regional online air quality modeling (AQM) system under NOAA's
21 Unified Forecast System (UFS), by assimilating measurements of fine particulate matter (PM_{2.5}, particles with
22 aerodynamic diameters less than 2.5 μm). PM_{2.5} assimilation is developed within the Joint Effort for Data
23 assimilation Integration (JEDI) framework and tested using its 3D-Var data assimilation (DA) component. The
24 PM_{2.5} observation operator is constructed by combining newly developed PM_{2.5} transformation recipes in the JEDI
25 Variable Derivation Repository (VADER) with a general spatial interpolation operator in the Unified Forward
26 Operator (UFO).

27 Cycled DA and forecast experiments were conducted from 1 to 21 September 2020, during a period of Western U.S.
28 wildfires, to assess the impact of assimilating PM_{2.5} observations from the AirNow and PurpleAir networks. The
29 control and analysis variables include individual aerosol species, with background error standard deviations
30 generated by scaling their respective background values. Prognostic variables such as aerosol particle number and
31 total particulate surface area are updated accordingly following each analysis update. All DA experiments use a
32 3-hourly cycling interval, with PM_{2.5} observations assimilated every 3 hours. The control experiment uses the same
33 configuration but without any data assimilation. Results show that assimilating either AirNow or PurpleAir PM_{2.5}

34 data reduces 1–24 h forecast errors in terms of mean absolute error (MAE) and root mean square error (RMSE)
35 compared to the control run over Continental United States (CONUS). Substantial improvements are in regions
36 where fire events took place and largely affected by transported smoke. Overall, the assimilation of PurpleAir
37 observations in addition to AirNow data leads to a slight reduction in 3–24 h MAE.

38 **1 Introduction**

39 Particulate matter with an aerodynamic diameter of 2.5 micrometers or smaller ($PM_{2.5}$) is a key contributor to poor
40 air quality in the United States, posing significant risks to public health and the environment, and contributing to
41 substantial loss of life (Cohen et al. 2017; Colmer et al. 2020; Huang et al., 2025). Over the past few decades, poor
42 air quality in the U.S. has contributed to over 100,000 premature deaths annually, far exceeding fatalities from all
43 other weather-related causes combined, which average around 500 per year (Huang et al., 2025). Given its public
44 health significance, $PM_{2.5}$ is one of the important pollutants used in calculating the Air Quality Index (AQI)—a
45 standardized system designed to communicate daily air pollution levels to the public at the U.S. Environmental
46 Protection Agency (EPA). Elevated $PM_{2.5}$ concentrations frequently result in "unhealthy" AQI ratings, triggering
47 health advisories and public warnings.

48 $PM_{2.5}$ in the United States originates from a range of both anthropogenic and natural sources. Anthropogenic
49 sources include agricultural activities and combustion processes, such as emissions from motor vehicles, power
50 plants, industrial facilities, and residential heating systems. Among natural sources, wildfires are a particularly
51 significant contributor, especially in the western United States, where their frequency and intensity have escalated
52 dramatically over the past two decades (Wen and Burke, 2021). According to the U.S. Environmental Protection
53 Agency (EPA), wildfires account for approximately 15% to 30% of total $PM_{2.5}$ emissions nationwide (EPA, 2017).
54 While national seasonal averages of $PM_{2.5}$ have generally declined, summer $PM_{2.5}$ concentrations in the western
55 U.S. have remained persistently high, primarily due to wildfire smoke (O'Dell et al., 2019). In addition to degrading
56 air quality, wildfires have caused widespread property loss. Since 2005, more than 129,000 homes, businesses, and
57 other structures have been destroyed by wildfire-related events
58 (<https://headwaterseconomics.org/natural-hazards/structures-destroyed-by-wildfire>, last access on February 18,
59 2026), underscoring the urgent need for more effective strategies in air quality monitoring, forecasting, and wildfire
60 management.

61 The National Oceanic and Atmospheric Administration (NOAA) has developed an advanced regional Air Quality
62 Modeling (AQM) prediction system within the Unified Forecast System (UFS) framework to enhance the accuracy
63 of air quality forecasts across the United States, particularly during wildfire events (Huang et al. 2025). The National
64 Air Quality Forecast Capability (NAQFC), operated by NOAA's National Weather Service (NWS), has been
65 providing operational air quality forecast guidance for over 20 years, with continuous inclusion of new capabilities.
66 Under NAQFC, the AQM version 7 was implemented and became operational on May 14, 2024. The system
67 features online coupling of atmospheric and chemical models, allowing dynamic interactions between meteorology

68 and atmospheric chemistry. This integration improves the representation of emissions and ensures real-time
69 feedback of meteorological fields that influence chemical transformations and the transport of pollutants in the
70 atmosphere. The UFS-AQM online system has consistently shown improved performance in simulating major
71 wildfire events, including the significant wildfires in the northwestern coastal regions of the U.S. in September
72 2020, and widespread smoke transport from Canadian wildfires in the summer of 2023. This system was officially
73 implemented on May 14, 2024 as NOAA's operational air quality prediction system (AQMV7), replacing the
74 previous offline-coupled Global Forecast System using the Finite Volume Cube-Sphere dynamical core (GFS-FV3)
75 version 15 with the Community Multiscale Air Quality modeling system (CMAQv5.0.2)(Chen et al. 2021).

76 PM_{2.5} data assimilation (DA) has proven effective in reducing errors in air quality forecasts (e.g., Pagowski et al.
77 2010, 2012; Schwartz et al. 2012; Wu et al. 2015; Robichaud 2017; Lee et al. 2021; Chen et al. 2022, Ha 2022;
78 Vogel et al. 2025, among others). Pagowski et al. (2010) demonstrated that fine aerosol forecasts benefit from
79 AirNow PM_{2.5} DA, showing improved verification scores for a period of at least 24 hours. Schwartz et al. (2012)
80 found that assimilating AirNow PM_{2.5} observations significantly improved surface PM_{2.5} forecasts over the
81 CONUS compared to forecasts without DA. Wu et al. (2015) reported that incorporating ground-based PM_{2.5}
82 observations notably enhanced 24-hour forecasts during a severe pollution episode in Shanghai. Similarly, Chen et
83 al. (2022) showed that assimilating multi-source PM_{2.5} data significantly improved WRF-Chem PM_{2.5} forecasts
84 with benefits lasting up to 48 hours. Lee et al. (2021) highlighted the effectiveness of assimilating ground in-situ
85 surface PM_{2.5} observations in improving the short-term PM_{2.5} predictions in Northeast Asia.

86 Many operational regional air quality prediction systems around the world use some form of data assimilation to
87 initialize the forecasts. These approaches vary in complexity, ranging from simple optimal interpolation to full
88 variational or ensemble Kalman filter methods (e.g. Robichaud et al. 2016; Wei et al. 2024; Colette et al. 2024). In
89 NOAA's current regional air quality model (AQM) operations, aerosol and chemical initial conditions are
90 "warm-started" using 6-hour forecasts from the previous model cycle. The implementation of an aerosol data
91 assimilation system can further enhance short-term air quality forecasts by providing more accurate spatial analyses
92 of initial aerosol distributions.

93 To establish aerosol data assimilation capabilities for NOAA's regional operational AQM system, we employ the
94 Joint Effort for Data assimilation Integration (JEDI) (Trémolet and Auligné, 2020). JEDI is a flexible, agnostic, and
95 modern data assimilation system applicable to a wide range of forecasting systems (e.g. Liu et al. 2023; Huang et al.
96 2023; Sluka, 2024). JEDI offers a platform that supports efficient scientific development and facilitates the transition
97 from research to operations. As part of a broader strategic shift, NOAA and partner agencies are transitioning their
98 data assimilation systems to JEDI, opening the door for rapid integration of new scientific advancements, greater
99 consistency across modeling systems, and enhanced collaboration across research communities and operational
100 centers.

101 This study aims to develop and evaluate an initial aerosol analysis capability for the NOAA's regional AQM system
102 by assimilating PM_{2.5} observations using the JEDI three-dimensional variational (3D-Var) data assimilation

103 framework. Compared to previous $PM_{2.5}$ data assimilation studies, this research adopts the NOAA’s regional
 104 operational AQMv7 system and incorporates a new $PM_{2.5}$ transform in JEDI for assimilating $PM_{2.5}$ observations. In
 105 addition to evaluating the impact of assimilating AirNow $PM_{2.5}$ measurements on air quality prediction, this study
 106 also examines the impact of assimilating low-cost PurpleAir observations. [Although PurpleAir data are valuable for
 107 \$PM_{2.5}\$ analysis \(White et al. 2026\) and real-time air quality monitoring, their potential impact on numerical air
 108 quality prediction remains insufficiently explored.](#) To the authors’ best knowledge, this is the first study to
 109 demonstrate the value of PurpleAir observations for air quality prediction [during the wildfires of September 2020](#)
 110 using the AQMv7 system.

111 The paper is organized as follows: section 2 provides a description of Methodology including the NOAA’s AQM
 112 system, 3D-Var approach, and JEDI $PM_{2.5}$ assimilation. Experimental setup is presented in section 3 including case
 113 description, AQM configuration, AirNow and PurpleAir $PM_{2.5}$ observations and background errors setup. Results
 114 are described in section 4. A summary and discussion are presented in the final section.

115 **2 Methodology**

116 **2.1 AQMv7 overview**

117 The NOAA’s regional operational AQMv7 system was developed through the online coupling of the Finite-Volume
 118 version 3 (FV3) dynamical core-based atmospheric model (Black et al 2021) with the EPA’s Community Multiscale
 119 Air Quality (CMAQ) model v5.2.0 within the UFS framework (Huang et al., 2025). In this UFS-AQM online
 120 system, CMAQ is treated as an atmospheric chemistry column model to simulate atmospheric chemistry reactions
 121 that govern concentrations of chemical species including gas- and aerosol-phase species. The transport terms of
 122 chemical species are handled by the FV3 dynamical core in the same way as other physics tracers (Huang et al.,
 123 2025). Aerosol module version 6 (AERO6) (Zhang et al. 2018) is utilized by CMAQ to simulate aerosol processes.

124 **2.2 $PM_{2.5}$ assimilation within JEDI 3D-Var**

125 In the JEDI framework, a series of components are provided to create a flexible, comprehensive data assimilation
 126 system (Trémolet. and Auligné, 2020). The JEDI 3D-Var component is used to assimilate $PM_{2.5}$ for AQMv7. The
 127 3D-Var method is chosen for its operational feasibility, primarily due to its low computational cost and the fact that
 128 it does not require an ensemble prediction system, as is needed in (hybrid) ensemble–variational data assimilation.

129 In practice, a 3D-Var data assimilation system typically uses an incremental approach to minimize a quadratic cost
 130 function which is defined in terms of the analysis increment δx relative to the guess state x_g :

$$131 J(\delta x) = \frac{1}{2} (\delta x - \delta x_g) B^{-1} (\delta x - \delta x_g)^T + \frac{1}{2} (\mathbf{H}[\delta x] - d) R^{-1} (\mathbf{H}[\delta x] - d)^T \quad (1)$$

132 Where:

- 133 • $\delta x_g = x_b - x_g$ is the guess state departure from background state x_b , which is usually taken from a
- 134 previous short-term forecast.
- 135 • \mathbf{H} is the linearized observation operator of nonlinear observation operator \mathbf{H} .
- 136 • \mathbf{B} and \mathbf{R} are the background and observation error covariance matrices, respectively.
- 137 • d is the innovation vector, defined as:

$$138 \quad d = y - H(x_g) \quad (2)$$

139 with y representing the observation vector.

140 Once the increment δx is obtained, the analysis state x^a is reconstructed as:

$$141 \quad x^a = x_g + \delta x \quad (3)$$

142 **2.2.1 PM_{2.5} observation operator**

143 To assimilate PM_{2.5} data, a PM_{2.5} transform that builds relationships between the model aerosol variables and the
 144 observed PM_{2.5} needs to be developed. In AQMv7, the modal approach taken in the CMAQ model represents
 145 aerosol particle size distributions as the superposition of three lognormal modes: Aitken (I), accumulation (J), and
 146 coarse (K). It predicts only three integral properties of the size distribution for each mode: the total particle number
 147 concentration, the total surface area concentration, and the total mass concentration of the individual chemical
 148 components.

149 The total PM_{2.5} concentration is calculated as a weighted sum of the individual aerosol concentration across these
 150 three modes:

$$151 \quad \text{PM}_{2.5} = \text{ATOTI} \cdot \text{PM25AT} + \text{ATOTJ} \cdot \text{PM25AC} + \text{ATOTK} \cdot \text{PM25CO} \quad (4)$$

152 Here, ATOTI, ATOTJ, and ATOTK represent the total aerosol mass concentrations in the Aitken, accumulation, and
 153 coarse modes, respectively. For example, ATOTI is the combined mass of 14 prognostic aerosol variables in the
 154 Aitken mode from the AERO6 aerosol module. Similarly, ATOTJ and ATOTK are the aggregated mass
 155 concentrations of 49 and 7 aerosol variables in the accumulation and coarse modes, respectively. PM25AT,
 156 PM25AC, and PM25CO are mass scaling factors for the three modes that vary by location and time. The aerosol
 157 variables within the same mode share the same mass scaling factor.

158 The PM_{2.5} observation operator is constructed by combining the newly developed PM_{2.5} transformation recipes in
 159 the JEDI Variable Derivation Repository (VADER) with an existing general spatial interpolation operator in the
 160 Unified Forward Operator (UFO). VADER is responsible for transforming model variables using user-defined
 161 “recipes” to generate new variables in model space. For PM_{2.5} assimilation, VADER computes PM_{2.5} from
 162 individual aerosol species using model-specific transformation, specifically using the equation 4 for this application.

163 Since $PM_{2.5}$ composition varies by model, these transforms are implemented within VADER to match the specific
164 structure of the regional air quality model AQMv7. Once $PM_{2.5}$ is derived in model space, UFO applies a generic
165 spatial interpolation operator to map the model-simulated values to the observation locations, enabling computation
166 of the observed minus forecast values.

167 The input for the $PM_{2.5}$ transformation are mixing ratio of the 70 aerosol variables with respect to dry air, the three
168 mass scaling factors in the three modes, and dry air density for unit conversion. The output is the $PM_{2.5}$ in unit
169 $\mu g/m^3$. It is noted that a new routine (recipe) has been added to VADER to derive dry air density from air
170 temperature, pressure, and the specific gas constant for the dry air using the ideal gas law. This is applied in cases
171 where the dry air density is not otherwise provided for the $PM_{2.5}$ calculation.

172 The new JEDI/VADER $PM_{2.5}$ recipe provides nonlinear (NL), tangent linear (TL), and adjoint (AD) transforms of
173 $PM_{2.5}$ that keeps the output products in the same grid space as the input variables. Hence, the generic interpolation
174 operator in UFO is used to connect the model-derived $PM_{2.5}$ fields with observed surface $PM_{2.5}$ measurements.
175 This respects the JEDI paradigm of keeping the UFO part of the JEDI model independent.

176 2.2.2 Background error covariance modeling

177 In a 3D-Var system, the background error covariance (BEC) determines both the spatial spreading of information
178 from observations and the magnitude of the analysis increments along with the observation error variance.

179 The background error covariance matrix B can be decomposed into a standard deviation matrix (Σ) and a correlation
180 matrix (C), as follows:

$$181 B = \Sigma C \Sigma \quad (5)$$

182 The correlation matrix C is generally non-diagonal. Σ is a diagonal matrix, with the standard deviations of the
183 background errors for each variable on the diagonal.

184 The error modeling of the correlation matrix and standard deviations usually apply to control variables. In the first
185 implementation of aerosol data assimilation in JEDI for AQMv7, the control variables are defined as individual
186 forecast aerosol variables, resulting in 70 control variables for AQMv7 with the AERO6 aerosol mechanism. The
187 setup of background error standard deviation and correlation modeling will be described in Section 3: Experimental
188 setup.

189 2.2.3 Minimization Algorithm (DRIPCG)

190 JEDI provides several minimization algorithm options. In this paper, we use the Derber–Rosati Inexact
191 Preconditioned Conjugate Gradient (DRIPCG) algorithm (Derber and Rosati, 1989), as implemented in the JEDI's

192 OOPS (Object-Oriented Prediction System) framework. DRIPCG has been extensively tested and is chosen here for
193 stability and convergence efficiency.

194 **3 Experimental setup**

195 **3.1 The September 2020 fire event and AQMv7 system setup**

196 The wildfires of September 2020 ranked among the most intense in the U.S. in recent years. These fires produced
197 dense smoke that initially moved westward over the Willamette Valley in western Oregon and eventually blanketed
198 the broader region. As a result, air quality rapidly across Oregon, Washington, and Idaho deteriorated to hazardous
199 levels, marking one of the worst air quality periods in recent decades (Mass et al., 2021). Wildfire smoke originating
200 from California, Oregon, and Washington was injected into the free troposphere and transported across the country
201 by prevailing winds, leading to hazy conditions in several states. According to Li et al. (2021), from August to
202 October 2020, wildfires in the western U.S. contributed 23% of surface $PM_{2.5}$ across CONUS, with higher
203 contributions observed along the Pacific Coast (43%) and in mountain region (42%). This study focuses on the peak
204 fire activity occurring between September 1 and 21.

205 In this research, the model configuration is almost the same as the operational AQMv7 setup except for running over
206 the CONUS domain with a 3 hourly cycling interval. The AQMv7 system is configured over the CONUS domain
207 with a grid-spacing of 13 km and 65 vertical levels, extending up to 0.2 hPa. The system uses the Global Forecast
208 System version 16 (GFSv16) physics package within the Common Community Physics Package (CCPP) framework
209 to generate the meteorological fields driving air quality predictions. Meteorological initial conditions and lateral
210 boundary conditions are generated using GFS forecast outputs with lead times up to 30 hours at 3-hour intervals
211 from the previous GFS cycle. Fire-related emissions are represented using real-time Regional hourly Advanced
212 Baseline Imager (ABI) and Visible Infrared Imaging Radiometer Suite (VIIRS) Emissions (RAVE) data at 0.03°
213 spatial resolution. Anthropogenic emissions are based on the 2016 U.S. EPA NEI Collaborative (NEIC2016v1)
214 modeling platform. Gas-phase chemistry is simulated using the Carbon Bond Mechanism version 6 (CB6r3) with
215 updated isoprene chemistry and revised photolysis rates. More detailed information including physics, chemistry
216 options, anthropogenic emissions, and fire emissions about the model configuration can be found in Huang et al.
217 (2025).

218 **3.2 $PM_{2.5}$ observations**

219 In this study, surface $PM_{2.5}$ observations were obtained from two sources: AirNow and PurpleAir observing
220 networks. These datasets differ in sensor type, spatial coverage, and quality control (QC) requirements. AirNow
221 provides regulatory-grade measurements from federal, state, and local monitoring stations, while PurpleAir is a
222 low-cost, community-based network of air quality sensors. PurpleAir sensors are widely deployed by individuals
223 and communities, providing real-time data on $PM_{2.5}$ concentrations as well as meteorological variables such as
224 temperature, pressure, and relative humidity. Only the data reported from outdoor $PM_{2.5}$ sensors are used in this

225 study. The PurpleAir data were available for registered users through the PurpleAir API.
226 (<https://community.purpleair.com/t/api-use-guidelines/1589>; last access on February 18 2026)

227 3.2.1 PurpleAir PM_{2.5} quality control

228 Quality control and correction of PurpleAir data followed the methodology described in Barkjohn et al. (2021).
229 Readers are referred to that paper for further details. The following quality control (QC) filters were applied to the
230 raw PurpleAir PM_{2.5} measurements:

- 231 • Reported PM_{2.5} values from two Plantower sensors within the PurpleAir sensor (channels A and B) must
232 be nonnegative.
- 233 • The PurpleAir sensor channel A and B consistency:
 - 234 ○ Absolute difference < 5 µg/m³, *or*
 - 235 ○ Relative difference within 61%.
- 236 • PM_{2.5} values must not exceed PM₁₀ values.
- 237 • PM_{2.5} values must be less than 3000 µg/m³ (upper threshold).
- 238 • Gross check of relative humidity with range 0-100%.

239 Only PurpleAir PM_{2.5} measurements that passed all the above QC criteria were retained for subsequent correction.

240 3.2.2 PurpleAir PM_{2.5} correction

241 A correction is required because the PurpleAir raw data usually overestimate PM_{2.5} concentrations under typical
242 ambient and smoke-impacted conditions. Correction of PurpleAir PM_{2.5} measurements was performed using a
243 multiple linear regression model based on sensor-reported PM_{2.5} (PA) and relative humidity (RH), following the
244 correction formula proposed by Barkjohn et al. (2021):

$$245 \text{PM}_{2.5} = 0.524 \times \text{PA} - 0.0862 \times \text{RH} + 5.75 \quad (6)$$

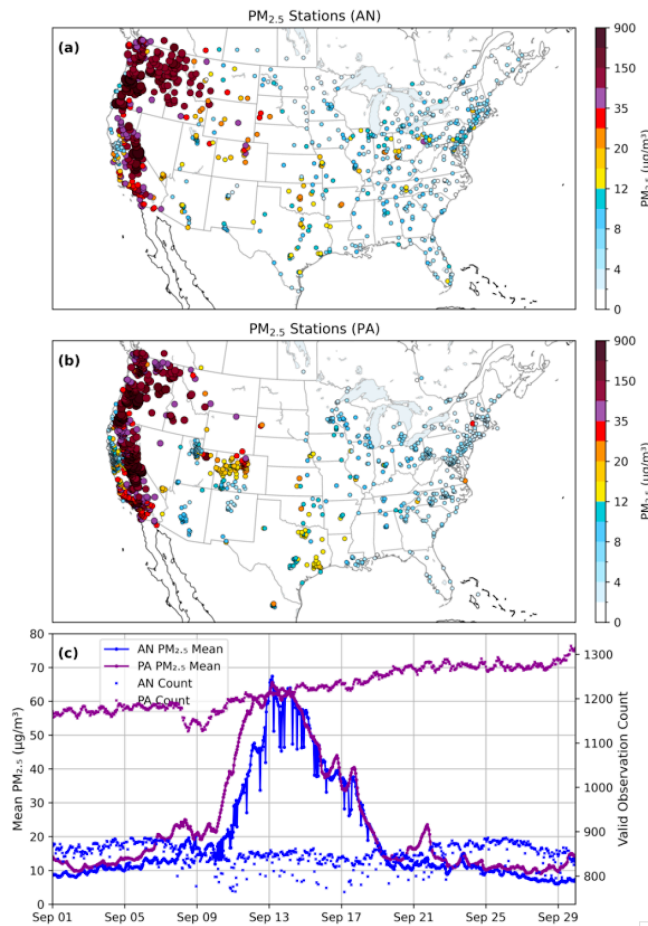
246 We adopt the above equation because it was United States-wide valid by fitting data from September 2017 until
247 January 2020. In addition, although the correction was originally derived for 24-hour averaged PM_{2.5}, it is
248 consistent with a regression equation obtained from the September 2020 dataset based on 1-hour averaged PM_{2.5}.

249 3.2.3 Observation error assignment

250 Observation error standard deviations were assigned to each network. The AirNow PM_{2.5} observation errors were
251 set to 5% of the observed values. For PurpleAir PM_{2.5} data, the observation errors were set to 10% of the observed
252 values to reflect the greater uncertainty typically associated with lower-cost sensors compared with regulatory
253 AirNow monitors. The 10% value is also consistent with the EPA definition of acceptable measurement uncertainty,
254 which specifies a 10% coefficient of variation for total precision.

255 3.2.4 Observation spatial distribution

256 Figure 1a–b shows the spatial distribution of AirNow and PurpleAir PM_{2.5} monitoring stations at 1200 UTC on
257 September 16, 2020. PurpleAir sensors are especially concentrated in densely populated areas, leading to notable
258 spatial variability in observation coverage during the September 2020 wildfire events. Coverage is particularly dense
259 in urban regions of the western United States (e.g. California, Oregon, Washington, Utah, Arizona and Colorado),
260 while rural and remote areas have significantly fewer sensors, for example, Nevada and North Dakota. Figure 1c
261 displays the time series of domain averaged PM_{2.5} values and station counts from the AirNow and PurpleAir
262 networks. The number of AirNow stations ranges from approximately 800 to 900, while PurpleAir stations number
263 between 1,160 and 1,300. Dropouts in the AirNow network lead to sudden decreases in station count and
264 corresponding drops in the PM_{2.5} time series. In contrast, the PurpleAir network shows a general upward trend in
265 station count, with no major data dropouts observed.



266

267 **Figure 1.** (a-b). Spatial distribution of AirNow(AN) and PurpleAir(PA) PM_{2.5} monitoring stations on 1200 UTC 16
268 September 2020. For PurpleAir, only stations that passed the quality control are shown. The displayed values are the
269 corrected concentrations calculated using Eq. (6). (c). Time series of domain averaged PM_{2.5} values and numbers
270 from AirNow and PurpleAir observing networks.

271 3.3 Background error covariance

272 In this study, the background error standard deviation (Σ) for each control variable is constructed based on the
273 background forecast; specifically, the error standard deviations of an aerosol variable are prescribed as proportional
274 to its background values.

275 The proportional scaling factor s is approximately estimated by building a linear relationship between the $PM_{2.5}$
276 standard error (Σ) and the background forecast $PM_{2.5}^{bkg}$ $PM_{2.5}$ concentrations:

$$277 \Sigma = s \cdot PM_{2.5}^{bkg} \quad (7)$$

278 The scaling factor s is subsequently applied to all $PM_{2.5}$ components, i.e., the 70 prognostic aerosol variables, to
279 construct their error standard deviations.

280 This proportionality-based approach has also been adopted in the MOCAGE operational system (Colette et al.,
281 2024), where background error standard deviations are similarly prescribed relative to background concentrations as
282 a first-order approximation.

283 Tang et al. (2023) tested a similar method, in which the background $PM_{2.5}$ error variance is first estimated using the
284 Hollingsworth–Lönnberg method (Hollingsworth and Lönnberg, 1986). A linear relationship is then established
285 between the estimated $PM_{2.5}$ standard error and the background forecast $PM_{2.5}^{bkg}$.

286 Here we take the same idea but using an alternative approach to roughly estimate the background $PM_{2.5}$ forecast
287 error variance. The background $PM_{2.5}$ error variance (Σ^2) is estimated using $PM_{2.5}$ innovation information d
288 defined in the subsection 2.2, and observation error information R specified in the subsection 3.2.3, specifically,
289 $\Sigma^2 = E(d d^T) - R$ (8)

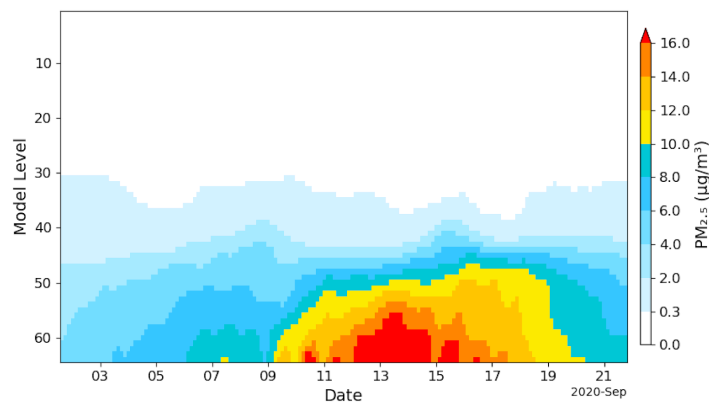
290 In Eq. 8, $E(\cdot)$ denotes the mathematical expectation operator. The superscript T denotes the transpose of a vector.
291 Equation 8 is valid under the assumption that observation and background errors are uncorrelated. This assumption
292 is reasonable when the innovation vector d is calculated using forecasts from a free-running model without any
293 aerosol data assimilation.

294 In this study, short-term (e.g., 3-hour) $PM_{2.5}$ forecasts from a free run conducted during 1–21 September 2020 were
295 used to compute the innovation vector d . This free run, referred to as the *control run*, is described in detail in the
296 following section. Using the innovations and observation errors from subsection 2.2 and 3.2.3 as inputs to Equation
297 8, the background error variance of $PM_{2.5}$ was first estimated. This error, along with the background values, was
298 then used in Equation 7 to estimate the scaling factor, s . This scaling factor was subsequently applied in all
299 assimilation experiments presented in this study.

300 This proportionality-based approach implicitly assumes that displacement errors [and severe background](#)
301 [underprediction errors](#) do not dominate, thereby focusing the assimilation process on correcting amplitude. It offers
302 several benefits:

- 303 • It helps constrain analysis increments to physically meaningful regions. For example, it prevents the
304 generation of sea salt aerosol increments over inland areas where no sea salt is present in the background.
305 This is a problem that can occur when using GSI’s height-dependent or latitude–height-dependent
306 background error variance formulations, particularly when individual aerosol species are used as control
307 variables.
- 308 • It introduces location- and time-dependent background error variance information, improving the realism of
309 background error specification. Moreover, the aerosol variables that dominate background errors vary by
310 location and assimilation cycle, rather than being consistently dominated by the same species when using
311 constant static background error statistics. For example, organic and black carbon typically exhibit the
312 largest errors in wildfire regions and downwind areas affected by smoke, whereas other regions may be
313 dominated by non-organic aerosols.

314 An example of domain averaged background $PM_{2.5}$ error standard deviation from a data assimilation run that
315 assimilated both AirNow and PurpleAir $PM_{2.5}$ is shown in Figure 2. This figure is intended to illustrate the main
316 difference to static constant background errors, though the actual errors used in the data assimilation experiments are
317 the errors of the individual aerosol control variables. It is obvious that this approach produces dynamically location-
318 and time-dependent varying error estimates that yields particularly large error variances during the peak fire events
319 from 10 to 20 September 2020.



320

321 **Figure 2.** Domain averaged $PM_{2.5}$ error standard deviations for the data assimilation run that assimilated both
322 AirNow and PurpleAir $PM_{2.5}$.

323 The background error correlation matrix C is modeled using a generic diffusion correlation operator designed for
324 short length scales, as implemented in the System-Agnostic Background Error Representation (SABER) repository
325 (Sluka, 2024). [The primary input parameters are the horizontal and vertical cutoff length scales, defined as the](#)

326 distances beyond which correlations are zero. A horizontal cutoff scale of 100 km is applied, consistent with
327 estimates derived from NMC statistics in previous GSI applications (Wang et al., 2021). For vertical correlations,
328 this study uses a cutoff length scale of 12 model levels, which helps confine the influence of surface PM_{2.5}
329 observations within the average daytime planetary boundary layer (PBL) height (~1450 m) and has demonstrated
330 improved surface PM_{2.5} prediction as will be discussed in Section 4.

331 3.4 Update of total particle number and surface area concentrations

332 After the aerosol mass concentration has been analyzed, total particle number concentration, total surface area
333 concentration can be updated accordingly. For simplicity, it is assumed that the ratio of the particle number
334 concentration to total particulate volume within each mode (I, J, K) remains the same as in the background. Total
335 particulate volume is used instead of mass mixing ratio because it is proportional to the particle number
336 concentration (see Eq. 3 in Binkowski and Roselle, 2003). A similar assumption was adopted by Li (2013) to update
337 number concentrations for the WRF-Chem model.

338 The number of particles is updated using the following relation:

$$339 N_a = N_b / V_b \times V_a \quad (9)$$

340 Where:

- 341 • N_a and N_b are the number of particles in the analysis and background, respectively, within each mode.
- 342 • V_a and V_b are the total particulate volumes in the analysis and background, respectively, within the same
343 mode.

344 The total particulate volume (V_a or V_b) within each mode is calculated by dividing the mass concentration of each
345 aerosol variable by its corresponding density in that mode, and then summing the results. This updating approach
346 implicitly assumes that changes in volume across the three modes are driven solely by variations in particle number,
347 rather than shifts in the aerosol size distribution. The total particulate surface area within each mode is then updated
348 using the same volume ratio, i.e., V_a / V_b (Eq. 9) multiplied by the background surface area.

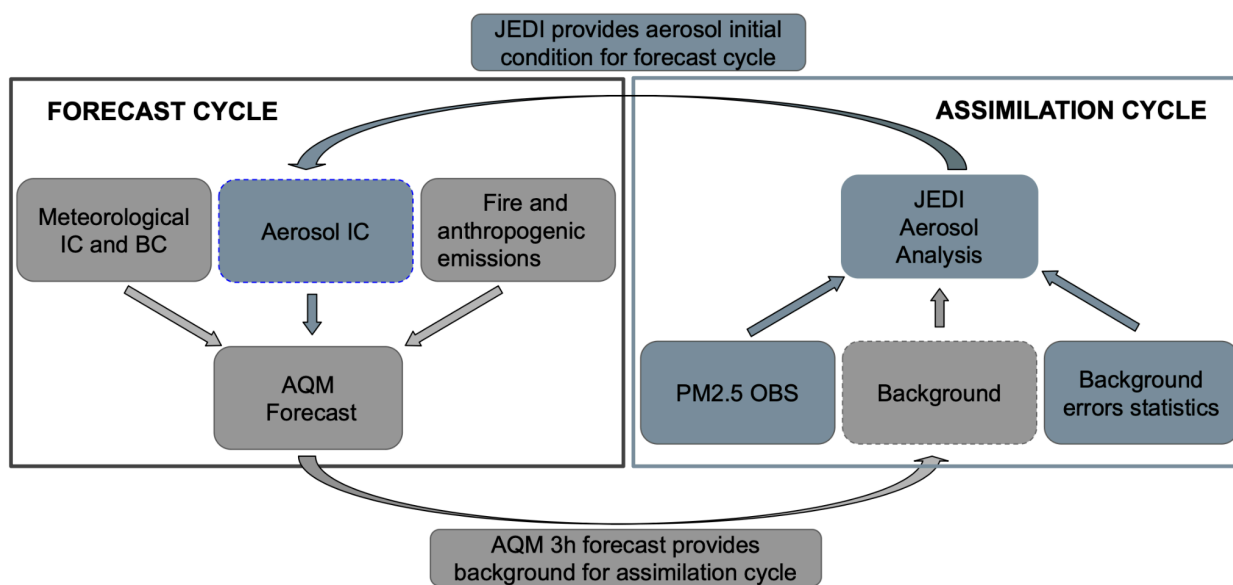
349 In preparatory work for this study, six-hourly cycling experiments (Wang et al., 2025) have shown that updating
350 these variables is crucial for improving AQMv7 performance. In contrast, previous work using GSI with earlier
351 developmental versions of AQM did not update these variables, primarily because those model versions were less
352 advanced than the current operational AQMv7. As a result, there was still significant room for improving prediction
353 skills.

354 **3.5 Experiments**

355 In the operational AQMv7 configuration, aerosol initial conditions (IC) are warm-started from a previous forecast
 356 cycle. In contrast, in cycling data assimilation and forecasting experiments, the data assimilation system provides
 357 aerosol initial conditions for the subsequent forecast, while the short-term (3-hour) forecast serves as the background
 358 for the next data assimilation cycle. A schematic of the data assimilation and forecasting cycles is shown in Fig. 3.

359 In the assimilation cycle, JEDI updates the aerosol analysis by combining PM_{2.5} observations with the background
 360 information. The updated aerosol analysis, together with meteorological initial conditions, emissions, and other
 361 inputs, is then used to initialize the subsequent forecasts in the forecast cycle. Note that the meteorological initial
 362 conditions are not updated by JEDI but are generated from GFS forecast outputs of the previous GFS cycle.

363



364

365 **Figure 3.** A schematic of the data assimilation and forecasting cycles.

366 Four experiments were conducted to evaluate the performance of JEDI/AQM PM_{2.5} DA. Table 1 provides a
 367 description of the experiments. The first experiment is a control run (CTR), in which meteorological initial and
 368 boundary conditions are updated every 3 hours, while chemical and aerosol fields are carried over from the 3-hour
 369 forecast of the previous cycle. The other three experiments incorporate data assimilation: DA_AN, DA_PA, and
 370 DA_ANPA, which assimilate AirNow PM_{2.5} only, PurpleAir PM_{2.5} only, and both AirNow and PurpleAir PM_{2.5}
 371 observations, respectively.

372 **Table 1. Descriptions of the experiments.**

Experiment	Data Assimilation	PM _{2.5} Observations Assimilated	Aerosol Fields
------------	-------------------	--	----------------

CTR	No	None	Carried over from previous cycle's 3-hour forecast
DA_AN	Yes	AirNow PM _{2.5} only	Updated by Assimilation
DA_PA	Yes	PurpleAir PM _{2.5} only	Updated by Assimilation
DA_ANPA	Yes	AirNow + PurpleAir PM _{2.5}	Updated by Assimilation

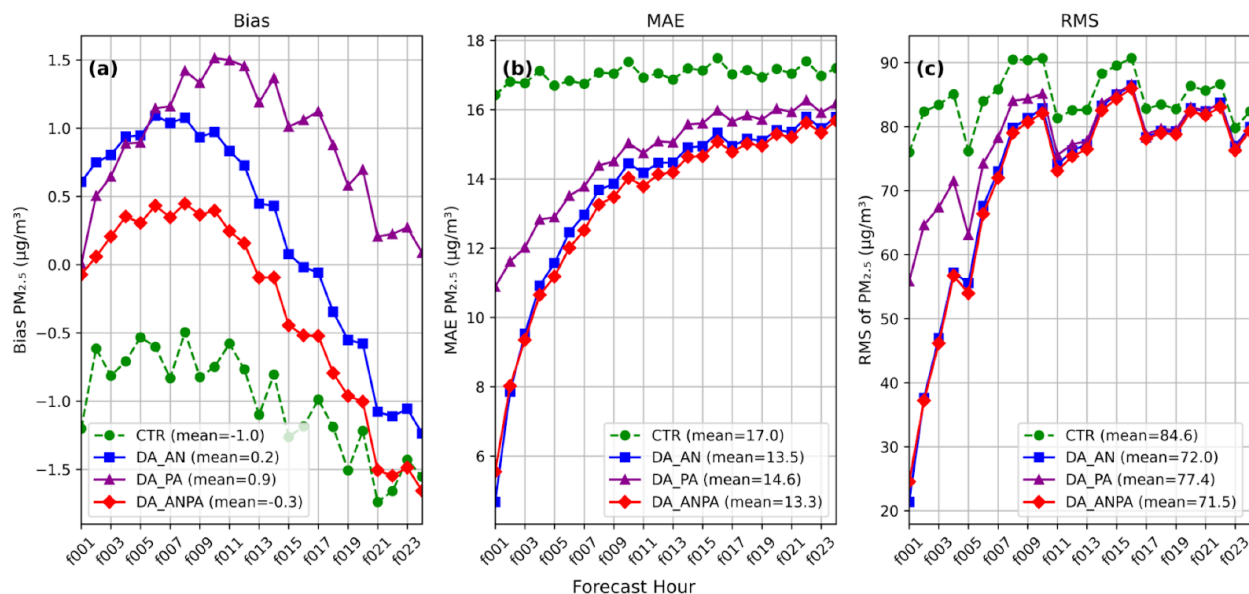
373 Like the CTR experiment, all DA experiments are conducted as 3-hourly cycling runs. Data assimilation is
 374 performed every 3 hours, and a 3-hour forecast is launched at each cycle. This 3-hour forecast serves as the
 375 background for the subsequent data assimilation and forecasting cycle. In addition, forecasts initialized at 0000,
 376 0600, 1200, and 1800 UTC are extended to 24 hours for evaluation purposes. The experimental period spans from
 377 1200 UTC on September 1 to 1800 UTC on September 21, 2020. It is noted that to reduce random sensor noise and
 378 improve comparability with the model resolution (~13 km), the PurpleAir PM_{2.5} data were spatially averaged onto a
 379 $0.1^\circ \times 0.1^\circ$ latitude–longitude grid [before assimilation](#).

380 4 Results

381 This section provides an overview of the impact of DA on PM_{2.5} forecasts. A total of 80 forecasts—initialized four
 382 times daily from 0000 UTC on September 2 to 1800 UTC on September 21, 2020—are used to evaluate model
 383 performance. AirNow PM_{2.5} observations are used to verify the forecast. Forecast errors are assessed using bias,
 384 mean absolute error (MAE), and root mean square error (RMSE). Forecast performance is evaluated using box plots,
 385 which illustrate the distribution, spread, and central tendency of forecast errors. Time series of PM_{2.5} at various
 386 forecast hours are presented to examine the temporal evolution of forecast performance. Additionally, spatial
 387 distributions of PM_{2.5} including observations, forecasts, forecast errors, and forecast differences are analyzed to
 388 evaluate the spatial impact of data assimilation on PM_{2.5} predictions.

389 Figure 4 presents the bias, mean absolute error (MAE), and root mean square error (RMSE) for the 1–24 h forecast
 390 of domain-averaged PM_{2.5}. Domain averages are computed over all states in the mainland United States. From the
 391 bias statistics (Fig. 4a), it is seen that the bias in the control run follows an upward trend initially, then reverses into a
 392 downward trend. The data assimilation runs show a similar trend, as data assimilation primarily corrects the model
 393 state and does not fully resolve inherent model bias. The control run underpredicted surface PM_{2.5} throughout the
 394 24-hour forecast period by about $1 \mu\text{g m}^{-3}$. This underprediction was improved in the data assimilation experiments.
 395 The two assimilated experiments, DA_AN and DA_ANPA, reduced the 1-24h mean bias to -0.2 and $-0.3 \mu\text{g m}^{-3}$,

396 respectively. The PurpleAir PM_{2.5} assimilation experiment (DA_PA) also slightly improved the 1-24h mean bias.
 397 It is seen that DA_PA produces a near zero bias at 1h forecast, however this is due to large positive and negative
 398 biases canceling out. Therefore, it should be used together with norms like Mean Absolute Error (MAE) and Root
 399 Mean Square Error (RMSE), which quantify the actual magnitude of forecast errors.
 400 In terms of MAE and RMSE, all the three data assimilation experiments reduced the surface PM_{2.5} forecast error
 401 throughout the 24-hour forecast period. The added value of assimilating PurpleAir PM_{2.5} data alongside AirNow
 402 observations is evident in the consistent MAE reduction (Fig. 4b). Its impact on RMSE (Fig. 4c) is also positive,
 403 though relatively small. Overall, all the data assimilation experiments show improved forecast skill compared to the
 404 control run.

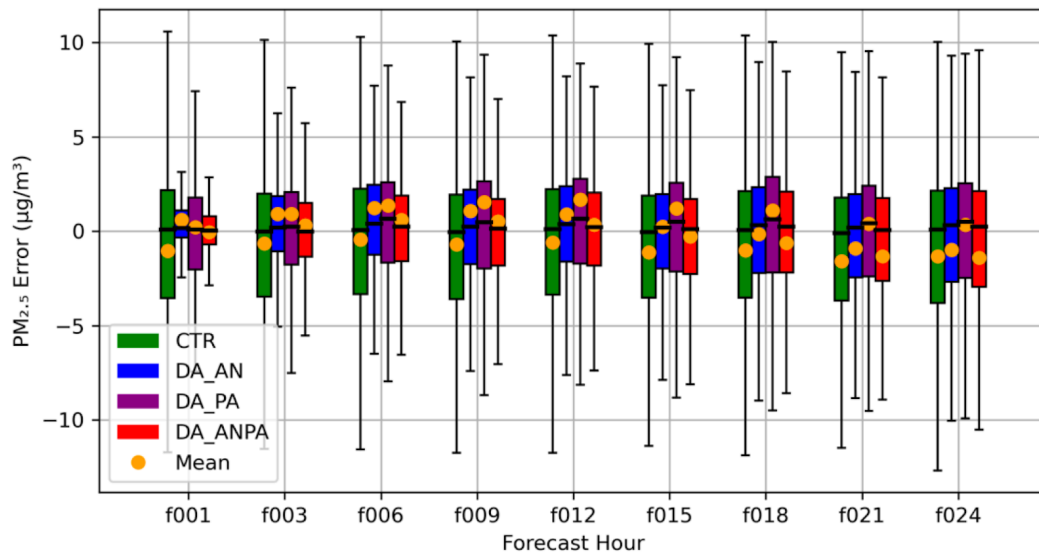


405
 406 **Figure 4.** PM_{2.5} forecast errors for 1–24 h lead times based on 80 forecasts initialized four times daily during
 407 September 2–21, 2020. Domain-averaged over CONUS. The x-axis represents forecast lead times from 1 to 24
 408 hours.

409 (a) Bias, (b) Mean Absolute Error (MAE), (c) Root Mean Square Error (RMSE).

410

411 Figure 5 shows box-and-whisker plots of PM_{2.5} forecast bias. Across all forecast hours, the interquartile range
 412 (IQR)—represented by the height of the boxes—is consistently smaller for the DA experiments compared to the
 413 control run. This indicates reduced forecast error spread between the 25th and 75th percentiles and suggests more
 414 consistent forecasts in the DA experiments. Although the median forecast bias in the control run is sometimes closer
 415 to zero, the DA_ANPA experiment performs comparably in terms of central tendency while showing clear
 416 improvements in reducing the mean forecast bias, as also reflected in Fig. 4a. Among the DA experiments, DA_AN
 417 and DA_ANPA show the most consistent improvement at 24-hour lead times, with DA_ANPA slightly
 418 outperforming others during the early forecast hours (e.g., hour 1 to 12). This suggests that assimilating PurpleAir
 419 observations in addition to AirNow helps reduce bias and brings the forecasts closer to observed PM_{2.5} values in the
 420 short term.

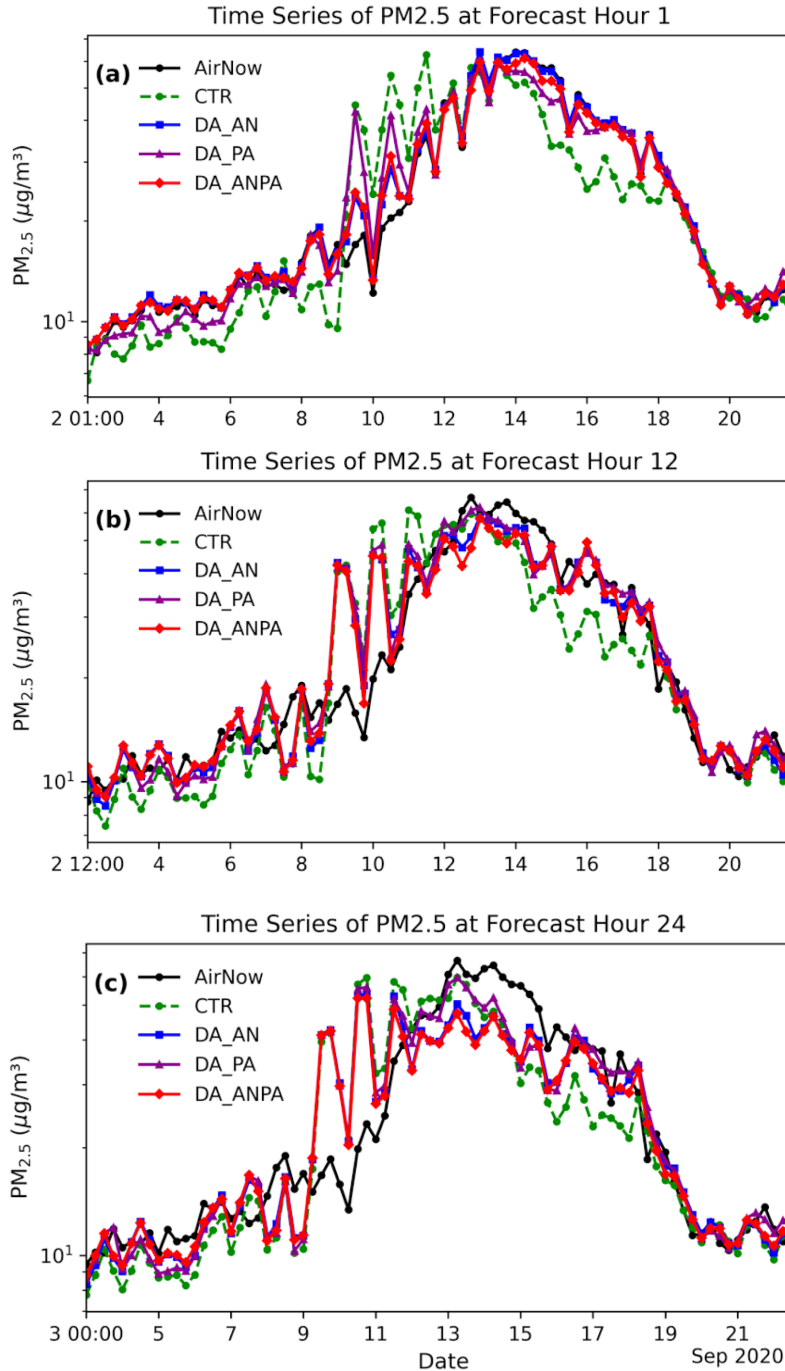


421

422 **Figure 5.** Box-and-whisker plot of PM_{2.5} forecast bias. Orange dot: domain averaged mean; Bottom edge = Q1
 423 (25th percentile); Top edge = Q3 (75th percentile); Height = Interquartile Range (IQR = Q3 – Q1); Horizontal line
 424 inside box: The median (50th percentile); Whiskers: Extend to the min and max values within $1.5 \times \text{IQR}$ from Q1
 425 and Q3.

426 Figure 6 shows time series of PM_{2.5} averaged over CONUS at forecast hours 1, 12, and 24, respectively. Consistent
 427 with the evaluations in Figures 4 and 5, all DA experiments generally improve PM_{2.5} forecasts. Notably, all DA
 428 experiments help correct underpredictions during September 2–9 and 14–17. In addition, the substantial
 429 overprediction during September 9–13 observed in the control run is partially mitigated by the DA experiments.
 430 Among the DA experiments, DA_AN and DA_ANPA show comparable performance and both outperform DA_PA.

431 While we have investigated the impact of DA on PM_{2.5} forecasts in terms of temporal evolution, it is also important
 432 to examine the spatial distribution of forecast fields, associated errors, and the impact of PM_{2.5} data assimilation.



433

434

435 **Figure 6.** Time series of $PM_{2.5}$ averaged over CONUS for (a) forecast hour 1, (b) forecast hour 12, and (c) forecast
 436 hour 24. The y-axis is shown on a logarithmic scale.

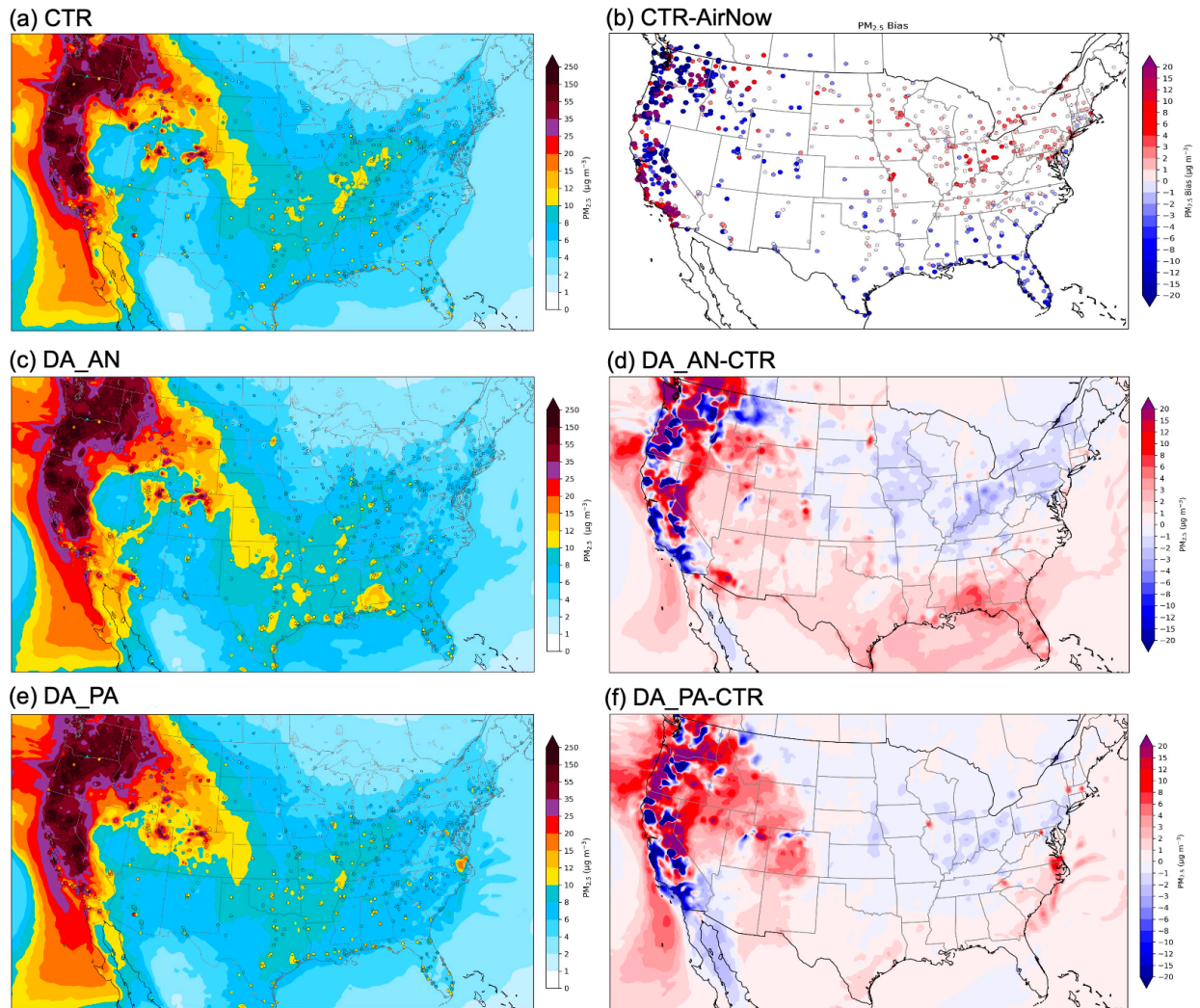
437 Figure 7 presents the spatial distribution of temporally averaged $PM_{2.5}$ forecasts at forecast hour 1, based on 80
 438 forecasts initialized four times daily (0000 UTC, 0600 UTC, 1200 UTC, and 1800 UTC) from September 2 to 21.
 439 The effects of wildfire events are clearly seen in Fig 7a, c and e across California, Oregon, and Washington—where
 440 the fires occurred—as well as in downstream regions such as Montana, Wyoming, Utah, and Colorado impacted by

441 smoke advection and transport.

442 1-h $\text{PM}_{2.5}$ forecast errors in the control run are evident in Fig. 6a but are more clearly highlighted in Fig. 7b, which
443 shows the difference between the control run and AirNow observations. Significant overpredictions appear along the
444 California coast, as well as in parts of the Midwest and Northeast U.S., including Tennessee, Kentucky, West
445 Virginia, and Virginia. Conversely, notable underpredictions are found over Colorado, New Mexico, much of Texas
446 and Oklahoma, and several Gulf Coast states.

447 Both DA_AN (Fig. 7c-d) and DA_PA (Fig. 7e-f) show similar spatial correction patterns across California, Oregon,
448 and Washington, particularly in reducing overpredictions along the California coast. They also produce comparable
449 large-scale adjustments across the Northeast, Midwest, and Southern U.S., with [their spatial patterns](#) (Fig. 7d and 7f)
450 largely opposite in sign to those in the CTR–AirNow difference (Fig. 7b). This indicates that both DA experiments
451 effectively mitigate the control run’s over- and underpredictions.

452 However, the magnitude of the corrections is generally smaller in DA_PA than in DA_AN. DA_PA shows its
453 strongest impact over Nevada, northern Utah, Colorado, and southwestern New Mexico, where it helps alleviate
454 regional underpredictions (Fig. 7e and 7f). These improvements are also observed in DA_ANPA, whose spatial
455 pattern closely resembles DA_AN except over these few states (figures not shown).



456

457 **Figure 7.** Spatial distribution of average $PM_{2.5}$ at forecast hour 1, based on 80 forecasts initialized four times daily
 458 (0000 UTC, 0600 UTC, 1200 UTC, and 1800 UTC) during 2–21 September.

459 (a) $PM_{2.5}$ in experiment CTR (shaded) overlaid with AirNow $PM_{2.5}$ observations (filled dots).

460 (b) $PM_{2.5}$ bias in experiment CTR.

461 (c) $PM_{2.5}$ in experiment DA_AN (shaded) overlaid with AirNow $PM_{2.5}$ observations.

462 (d) $PM_{2.5}$ difference between experiments DA_AN and CTR.

463 (e) $PM_{2.5}$ in experiment DA_PA (shaded) overlaid with AirNow $PM_{2.5}$ observations.

464 (f) $PM_{2.5}$ difference between experiments DA_PA and CTR.

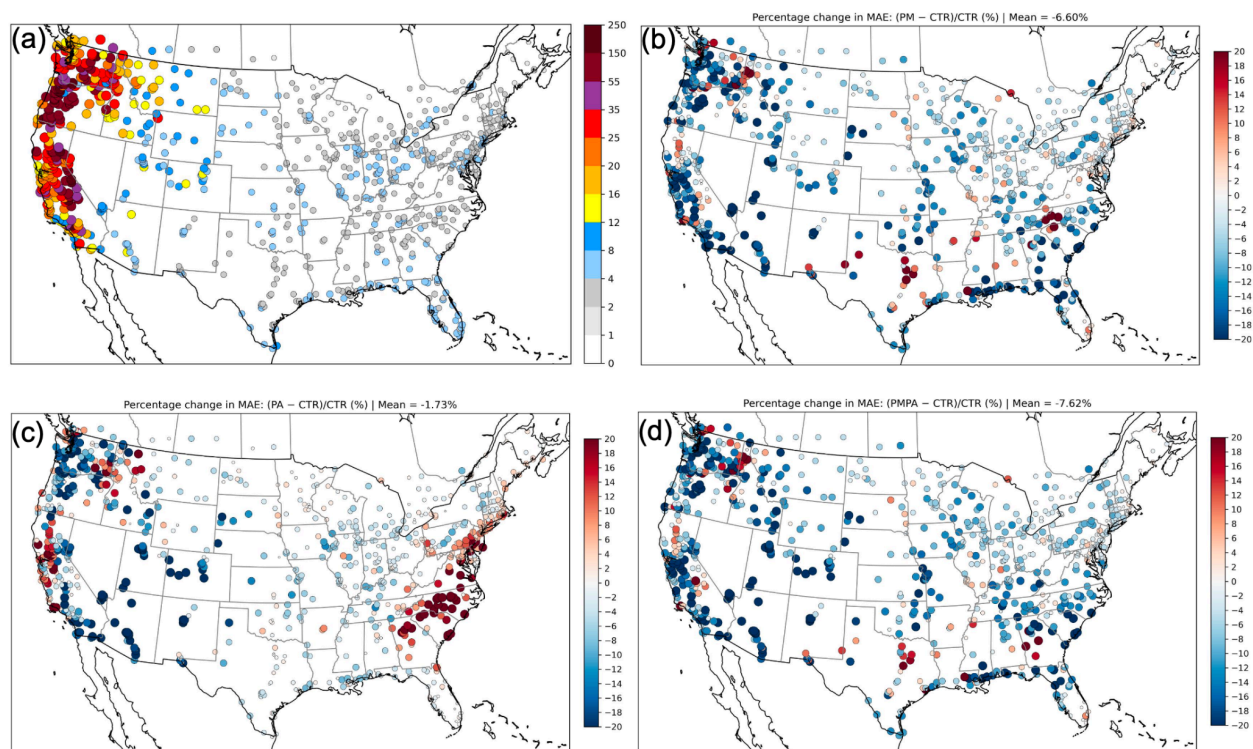
465 The above analysis shows that data assimilation effectively corrects the 1-h forecast errors in the control run,

466 particularly in the DA_AN and DA_ANPA experiments. It is therefore of interest to examine how data assimilation

467 affects longer forecast lead times. Figure 8 presents the MAE from the CTR experiment and the percentage change

468 in MAE (%) between the data assimilation (DA) experiments and the CTR experiment at the 24-h forecast lead time.

469 Negative values in Figs. 8b–d indicate a reduction in MAE.



470

471 **Figure 8.** (a) MAE from the control (CTR) experiment.

472 Percentage change in MAE (%) relative to CTR for (b) DA_AN, (c) DA_PA, and (d) DA_ANPA. The percentage
473 change is calculated as $(MAE(DA) - MAE(CTR)) / MAE(CTR) \times 100$.

474 It is seen from Fig. 8a that the largest MAE values occur in California, Oregon, Washington, Idaho, Montana,
475 Wyoming, Utah, Colorado, and Arizona. The $PM_{2.5}$ MAE in these states is generally greater than $10 \mu g m^{-3}$, with
476 maximum values exceeding $150 \mu g m^{-3}$ at certain stations in California, Oregon, and Washington. In contrast,
477 regions less affected by wildfire smoke exhibit MAE values below $10 \mu g m^{-3}$.

478 All DA experiments (Figs. 8b–d) show overall reductions in MAE at most stations. MAE reduction varies by
479 location, with substantial improvements observed in regions with large forecast errors, such as California, Oregon,
480 Washington, and Idaho, where MAE is reduced by approximately 20%. On average, assimilation of AirNow $PM_{2.5}$
481 observations alone significantly improves the 24-h forecast skill, with MAE reductions of 6.6% based on MAE
482 percentage changes averaged over all stations. In contrast, assimilation of PurpleAir data alone reduces the MAE by
483 only 1.7%. Assimilating both AirNow and PurpleAir $PM_{2.5}$ observations reduces the MAE by 7.6%, indicating that
484 PurpleAir data provides complementary value to AirNow in improving forecast skill.

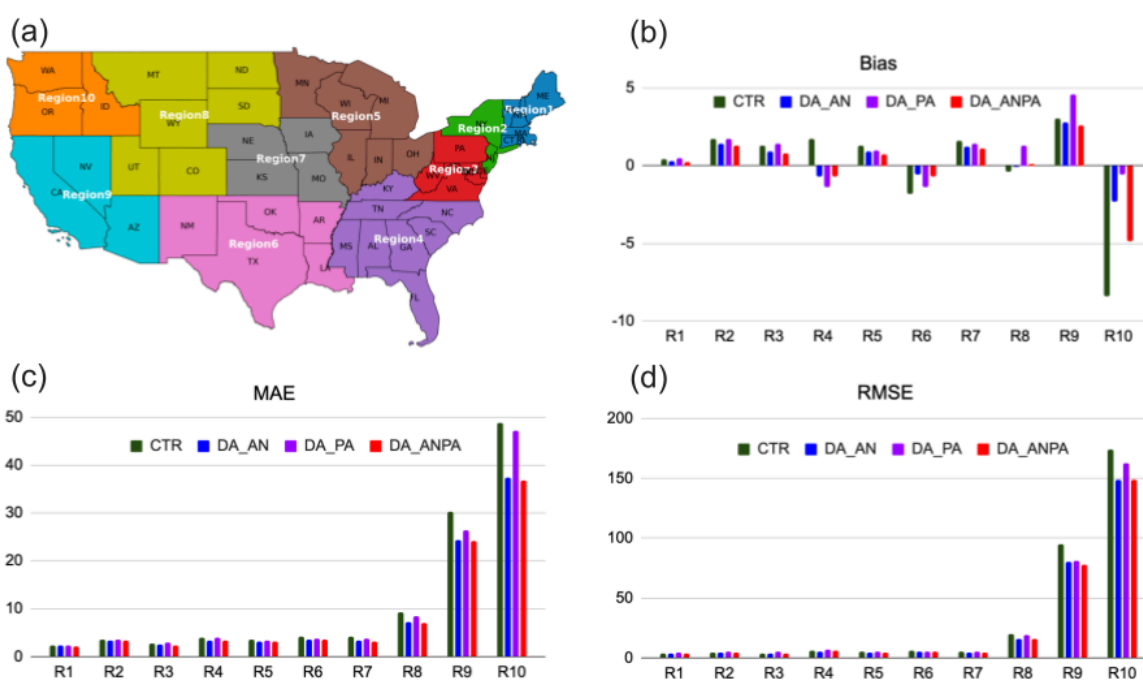
485 In the DA_PA experiment, a few eastern coastal states from Georgia to Virginia exhibit large percentage increases in
486 MAE. These increases are associated with relatively small absolute errors, as MAE values in the CTR experiment
487 over these states are typically only $2\text{--}4 \mu g m^{-3}$ (Fig. 8a). Increased MAE is also present at several stations at the 1-h
488 forecast lead time in the DA_PA experiment in these areas (figure not shown). In contrast, the MAE increase at the

489 24-h forecast lead time is much less pronounced in the experiment assimilating only AirNow PM_{2.5} observations.
 490 This behavior suggests potential quality issues in the assimilated PurpleAir data in those areas that require further
 491 investigation, although a contribution from model errors cannot be ruled out.

492 To further examine model performance across different regions, error statistics (bias, MAE, and RMSE) for the
 493 averaged 1–24 h PM_{2.5} forecasts from the control and data assimilation experiments over the 10 EPA regions are
 494 analyzed. Figure 9 presents the EPA Regions 1-10 and Averaged 1–24 h PM_{2.5} forecasts errors statistics in each
 495 EPA region.

496 In terms of bias (Fig. 9b), the DA_AN and DA_ANPA forecasts show improved performance relative to the control
 497 run. The DA_PA experiment also improves bias over most EPA regions, except for increased overprediction in EPA
 498 regions 8 and 9. For MAE and RMSE, the DA_AN and DA_ANPA experiments generally show improved
 499 performance across all EPA regions. The DA_PA experiment also exhibits improved, or at least comparable, MAE
 500 relative to the control run. However, DA_PA shows slightly increased RMSE over EPA regions 1–4, while reduced
 501 RMSE is found over other EPA regions.

502 Substantial reductions in MAE and RMSE are observed over EPA regions 8–10, where fire events occurred and/or
 503 where regions were most influenced by transported smoke. This is consistent with the large 1-h MAE reduction
 504 shown in Fig. 8. Notably, the DA_PA experiment, which assimilates PA observations alone, reduces both MAE and
 505 RMSE over EPA regions 8–10. Assimilating PurpleAir data together with AirNow data results in slightly smaller
 506 MAE and RMSE over these regions, suggesting that PurpleAir observations nonetheless provide complementary
 507 information to AirNow in these regions.



508

509 **Figure 9.** (a) EPA Regions 1-10. Averaged 1–24 h PM_{2.5} forecasts errors: (b) Bias, (c) MAE and (d) RMSE.

510 **5 Summary and discussion**

511 The latest version of NOAA's regional AQM system became operational on May 14, 2024. This system is based on
512 the online coupling of [the FV3 atmospheric model with the CMAQ model within the UFS framework](#). To improve
513 initial conditions for AQM and enhance predictions of wildfire impacts on air quality, the capability to assimilate
514 PM_{2.5} observations into AQMv7 was developed within JEDI and evaluated using its 3D-Var assimilation
515 component in this study. The developed assimilation scheme can also be used to generate analysis (reanalysis)
516 dataset for other applications, for example, providing data for training artificial intelligent models used in air quality
517 prediction.

518 Data assimilation experiments were conducted for the September 2020 Western U.S. wildfire episode, using
519 3-hourly cycling with observations from the AirNow and PurpleAir networks. In the data assimilation experiments,
520 the location- and time-dependent background error standard deviations of an aerosol variable are specified as
521 proportional to its background values, using a diagnosed scaling factor. In addition to updating the analyzed aerosol
522 variables in each mode, the particle number concentration and surface area of each mode are also updated. The
523 results show that assimilating AirNow PM_{2.5} observations improves 1–24 h forecast skill. Assimilating PurpleAir
524 data alone yields modest improvements in MAE. Combining PurpleAir with AirNow observations provides
525 additional benefit by slightly further reducing MAE relative to AirNow-only assimilation, indicating that PurpleAir
526 observations nonetheless provide complementary information to AirNow. The AirNow data assimilation alone or
527 with PurpleAir data generally show reduced MAE and RMSE across all EPA regions, whereas the largest reductions
528 in MAE and RMSE are observed over regions affected by fire events and/or strongly influenced by transported
529 smoke. The positive impact of PurpleAir data assimilation on smoke prediction during the September 2020 wildfires
530 has also been demonstrated in an experimental Rapid Refresh Forecast System coupled with the Smoke and Dust
531 Model (Wang et al., 2023), where it significantly reduced the model's 24-h underprediction of surface PM_{2.5}. Given
532 that PurpleAir data coverage has improved since September 2020, the results of this study further highlight its
533 potential to complement AirNow observations by filling spatial gaps and improving PM_{2.5} analysis and forecast
534 skill.

535 In this initial development and evaluation of aerosol data assimilation in JEDI for AQMv7, the control variables are
536 defined as individual forecast aerosol variables. In previous work on aerosol data assimilation for an earlier version
537 of AQM using the GSI system (Wang et al., 2021), one option for the control variables was to define them as the
538 total aerosol mass in each of the three modes, resulting in just three control variables. A control variable transform
539 was then applied to partition the analysis increments across these modes to individual aerosol species, based on the
540 ratio of each species' mass to the total mass within the corresponding mode. The use of total aerosol mass in the
541 three modes as control variables—thereby reducing the number of control variables from 70 to 3—is planned for a
542 future phase of development. The use of total masses as control variables also reduces the cost of the background
543 error statistics calculation and iterative minimization (Kumar et al. 2019).

544 This study focused on surface-level PM_{2.5} and did not incorporate vertical profile constraints with satellite-based
545 aerosol optical depth (AOD) retrievals, which could further enhance forecast skill. A key challenge is the need for a
546 robust forward operator in the CRTM AOD module—specifically, the creation and validation of lookup tables
547 (LUTs) for AOD calculations with AQM. As an intermediate solution, existing LUTs in CRTM, such as the GEOS-5
548 LUTs, have been tested by grouping and mapping AQM aerosol species to those used in GEOS-5 (Wang et al.
549 2025). AOD assimilation also depends on an accurate vertical distribution of aerosols in the background field so that
550 the CRTM AOD operator can provide meaningful gradient information at the correct vertical levels to constrain the
551 analysis update. However, AQM models have shown deficiencies for the September 2020 fire events in representing
552 smoke concentrations at and above plume rise levels, largely due to how fire emissions are injected into the model.
553 This will be improved in the next update of the operational AQM.

554 **Code and data availability**

555 The AQMV7 model, JEDI software and PM_{2.5} and fire emission data we used in this research are publicly available
556 on on Zenodo (<https://doi.org/10.5281/zenodo.17049857>; Wang et al., 2025b).

557 Users are referred to the guidance on compiling and running the model:
558 <https://ufs-srweather-app.readthedocs.io/en/develop/UsersGuide/index.html> (Last accessed on August 26, 2025).

559 Global Forecast System analysis data were downloaded from the NCAR Research Data Archive:
560 <https://doi.org/10.5065/D65D8PWK> (last access: Aug 26 2025)

561 **Author contribution**

562 HW designed and developed the PM_{2.5} DA capability within JEDI for the AQM model, conducted experiments, and
563 evaluated performance; CM and JB contributed to PM_{2.5} DA methodology, advised on code implementation, and
564 assisted in performance analysis; SW contributed to PM_{2.5} DA methodology and experimental design; RL
565 conducted control experiments and contributed to workflow development; JL and KW contribute to model
566 configuration and control run setup; YT contributed to background error modeling and observational error
567 specification; HC, AT and HL contributed to workflow development; JL performed quality control and correction of
568 PurpleAir observations.

569 **Competing interests**

570 The authors declare that they have no conflict of interest.

571 **Acknowledgements**

572 The authors sincerely thank Dr. Ming Hu and the three anonymous reviewers for their constructive comments and
573 insightful suggestions, which significantly improved the quality and clarity of this manuscript. The authors also
574 thank Dr. Mohammed Farooqui at Texas A&M University-Kingsville for assisting with Python scripts to download
575 the PurpleAir observations.

576 This research was supported by the Fire Weather and Precipitation Research and Development in Support of the
577 Disaster Relief Supplemental Appropriations Act (DRSA) project (NA23OAR4050200D), and in part by a NOAA
578 Cooperative Agreement NA22OAR4320151 with the University of Colorado. The scientific results and conclusions,
579 as well as any views or opinions expressed herein, are those of the authors and do not necessarily reflect those of
580 NOAA or the Department of Commerce.

581 References

- 582 Abatzoglou, J. T., Rupp, D. E., O'Neill, L. W., & Sadegh, M. (2021). Compound extremes drive the western
583 Oregon wildfires of September 2020. *Geophysical Research Letters*, 48(8), e2021GL092520.
584 <https://doi.org/10.1029/2021gl092520>
- 585 Albores, I. S., Buchholz, R. R., Ortega, I., Emmons, L. K., Hannigan, J. W., Lacey, F., et al. (2023).
586 Continental-scale atmospheric impacts of the 2020 western US wildfires. *Atmospheric Environment*, 294,
587 119436. <https://doi.org/10.1016/j.atmosenv.2022.119436>
- 588 Barkjohn, K. K., Gantt, B., and Clements, A. L.: Development and application of a United States-wide
589 correction for PM_{2.5} data collected with the PurpleAir sensor, *Atmos. Meas. Tech.*, 14, 4617–4637,
590 <https://doi.org/10.5194/amt-14-4617-2021>, 2021.DOI: 10.5194/amt-2020-413
- 591 Black, T. L., Abeles, J. A., Blake, B. T., Jovic, D., Rogers, E., Zhang, X., et al. (2021). A limited area modeling
592 capability for the finite-volume cubed-sphere (FV3) dynamical core and comparison with a global two-way
593 nest. *Journal of Advances in Modeling Earth Systems*, 13(6), e2021MS002483.
594 <https://doi.org/10.1029/2021MS002483>
- 595 Binkowski, F. S., and S. J. Roselle, Models-3 Community Multiscale Air Quality (CMAQ) model aerosol
596 component, 1, Model description, *J. Geophys. Res.*, 108(D6), 4183, doi:10.1029/2001JD001409, 2003.
- 597 Chen L, Mao F, Hong J, Zang L, Chen J, Zhang Y, Gan Y, Gong W, Xu H. Improving PM_{2.5} predictions during
598 COVID-19 lockdown by assimilating multi-source observations and adjusting emissions. *Environ Pollut.* 2022
599 Mar 15;297:118783. doi: 10.1016/j.envpol.2021.118783. Epub 2021 Dec 30. PMID: 34974086; PMCID:
600 PMC8717716.
- 601 Chen, X., Zhang, Y., Wang, K., Tong, D., Lee, P., Tang, Y., Huang, J., Campbell, P. C., Mcqueen, J., Pye, H. O.
602 T., Murphy, B. N., and Kang, D.: Evaluation of the offline-coupled GFSv15–FV3–CMAQv5.0.2 in support of
603 the next-generation National Air Quality Forecast Capability over the contiguous United States, *Geosci. Model*
604 *Dev.*, 14, 3969–3993, <https://doi.org/10.5194/gmd-14-3969-2021>, 2021.

605 Colette, A., Collin, G., Besson, F., and coauthors.: Copernicus Atmosphere Monitoring Service – Regional Air
606 Quality Production System v1.0, EGU sphere [preprint], <https://doi.org/10.5194/egusphere-2024-3744>, 2024.

607 Derber, J. C., and A. Rosati, 1989: A global ocean data assimilation system. *J. Phys. Oceanogr.*, **19**, 1333–1347,
608 [https://doi.org/10.1175/1520-0485\(1989\)019<1333:AGODAS>2.0.CO;2](https://doi.org/10.1175/1520-0485(1989)019<1333:AGODAS>2.0.CO;2).

609 Cohen, A. J., Brauer, M., Burnett, R., Anderson, H. R., Frostad, J., Estep, K., Balakrishnan, K., Brunekreef, B.,
610 Dandona, L., Dandona, R., Feigin, V., Freedman, G., Hubbell, B., Jobling, A., Kan, H., Knibbs, L., Liu, Y.,
611 Martin, R., Morawska, L., Pope III, C. A., Shin, H., Straif, K., Shaddick, G., Thomas, M., van Dingenen, R.,
612 van Donkelaar, A., Vos, T., Murray, C. J. L., and Forouzanfar, M. H.: Estimates and 25-year trends of the global
613 burden of disease attributable to ambient air pollution: an analysis of data from the Global Burden of Diseases
614 Study 2015, *Lancet*, **389**, 1907–1918, 2017.

615 Colmer, J., Hardman, I., Shimshack, J., and Voorheis, J.: Disparities in PM_{2.5} air pollution in the United States,
616 *Science*, 369(6503), 575–578, <https://doi.org/10.1126/science.aaz9353>, 2020.

617 Desroziers, G., L. Berre, B. Chapnik, and P. Poli. 2005. Diagnostic of observation, background and
618 analysis-error statistics in observation space. *Q. J. R. Meteorol. Soc.* 131:3385–96.
619 doi:10.1256/qj.05.108.doi:10.1256/qj.05.108

620 Ha, S.: Implementation of aerosol data assimilation in WRFDA (v4.0.3) for WRF-Chem (v3.9.1) using the
621 RACM/MADE-VBS scheme, *Geosci. Model Dev.*, 15, 1769–1788, <https://doi.org/10.5194/gmd-15-1769-2022>,
622 2022.

623 Hollingsworth, A., and P. Lönnberg. 1986. The statistical structure of short-range forecast errors as determined
624 from radiosonde data. Part I: The wind field. *Tellus A38*:111–36. doi:10.1111/j.1600-0870.1986.tb00460.x

625 Huang, J., I. Stajner, R. Montuoro, F. Yang, K. Wang, H.-C. Huang, C.-H. Jeon, B. Curtis, J. McQueen, H. Liu,
626 B. Baker, D. Tong, Y. Tang, P. Campbell, G. Grell, G. Frost, R. Schwantes, S. Wang, S. Kondragunta, F. Li, Y.
627 Jung. Development of the next-generation air quality prediction system in the unified forecast system
628 framework: enhancing predictability of wildfire air quality impacts. *Bull. Am. Meteorol. Soc.* (2025),
629 10.1175/BAMS-D-23-0053.1

630

631 Environmental Protection Agency. Technical Note on Reporting PM_{2.5} Continuous Monitoring and Speciation
632 Data to the Air Quality System (AQS). November 8, 2006.
633 [https://www.epa.gov/aqs/aqs-memos-technical-note-reporting-pm25-continuous-monitoring-and-speciation-data](https://www.epa.gov/aqs/aqs-memos-technical-note-reporting-pm25-continuous-monitoring-and-speciation-data-air-quality)
634 [-air-quality](https://www.epa.gov/aqs/aqs-memos-technical-note-reporting-pm25-continuous-monitoring-and-speciation-data-air-quality).

635 EPA (2017). Wildfire and Air Quality. U.S. Environmental Protection Agency.

636 Huang, B., Pagowski, M., Trahan, S., Martin, C. R., Tangborn, A., Kondragunta, S., & Kleist, D. T. (2023).
637 JEDI-based three-dimensional Ensemble-Variational Data Assimilation System for global aerosol forecasting at

638 NCEP. *Journal of Advances in Modeling Earth Systems*, 15(4), e2022MS003232.
639 <https://doi.org/10.1029/2022MS003232>

640 Lee Sojin, Chul Han Song, Kyung Man Han, Daven K. Henze, Kyunghwa Lee, Jinhyeok Yu, Jung-Hun Woo,
641 Jia Jung, Yunsoo Choi, Pablo E. Saide, Gregory R. Carmichael, Impacts of uncertainties in emissions on aerosol
642 data assimilation and short-term PM_{2.5} predictions over Northeast Asia, *Atmospheric Environment*, Volume
643 271, 2022, 118921, ISSN 1352-2310, <https://doi.org/10.1016/j.atmosenv.2021.118921>.

644 Li, Y., Tong, D., Ma, S., Zhang, X., Kondragunta, S., Li, F., & Saylor, R. (2021). Dominance of wildfires impact
645 on air quality exceedances during the 2020 record-breaking wildfire season in the United States. *Geophysical*
646 *Research Letters*, 48(21), e2021GL094908. <https://doi.org/10.1029/2021GL094908>

647 Li, Z., Zang, Z., Li, Q. B., Chao, Y., Chen, D., Ye, Z., Liu, Y., and Liou, K. N.: A three-dimensional variational
648 data assimilation system for multiple aerosol species with WRF/Chem and an application to PM_{2.5} prediction,
649 *Atmos. Chem. Phys.*, 13, 4265–4278, <https://doi.org/10.5194/acp-13-4265-2013>, 2013.

650 Liu, Z., Snyder, C., Guerrette, J. J., Jung, B.-J., Ban, J., Vahl, S., Wu, Y., Trémolet, Y., Auligné, T., Ménérier,
651 B., Shlyaeva, A., Herbener, S., Liu, E., Holdaway, D., and Johnson, B. T.: Data assimilation for the Model for
652 Prediction Across Scales – Atmosphere with the Joint Effort for Data assimilation Integration (JEDI-MPAS
653 1.0.0): EnVar implementation and evaluation, *Geosci. Model Dev.*, 15, 7859–7878,
654 <https://doi.org/10.5194/gmd-15-7859-2022>, 2022.

655 Kumar, R., Monache, L. D., Bresch, J., Saide, P. E., Tang, Y., Liu, Z., Silva, A. M. da, Alessandrini, S., Pfister,
656 G., Edwards, D., Lee, P., and Djalalova, I.: Toward Improving Short-Term Predictions of Fine Particulate Matter
657 Over the United States Via Assimilation of Satellite Aerosol Optical Depth Retrievals, *J. Geophys. Res.-Atmos.*,
658 124, 2753–2773, <https://doi.org/10.1029/2018JD029009>, 2019.

659 Mass, C.F.; Ovens, D.; Conrick, R.; Saltenberger, J. The September 2020 wildfires over the Pacific Northwest.
660 *Weather Forecast.* **2022**, 36, 1843–1865.

661 Ménard, R., Deshaies-Jacques, M., & Gasset, N. (2016). A comparison of correlation-length estimation methods
662 for the objective analysis of surface pollutants at Environment and Climate Change Canada. *Journal of the Air*
663 *& Waste Management Association*, 66(9), 874–895. <https://doi.org/10.1080/10962247.2016.1177620>

664 O'Dell, K. et al. (2019). Open-access study on wildfire smoke and PM_{2.5} trends in the western U.S.

665 Robichaud, A. (2017). Surface data assimilation of chemical compounds over North America and its impact on
666 air quality and Air Quality Health Index (AQHI) forecasts. *Air Quality, Atmosphere & Health*, 10(8), 955–970.
667 <https://doi.org/10.1007/s11869-017-0485-9>

668 National Centers for Environmental Prediction/National Weather Service/NOAA/U.S. Department of
669 Commerce: NCEP GFS 0.25 Degree Global Forecast Grids Historical Archive, Research Data Archive at the

670 National Center for Atmospheric Research, Computational and Information Systems Laboratory [data set],
671 <https://doi.org/10.5065/D65D8PWK> (last access: 26 August 2025).

672 Robichaud A, Ménard R, Zaitseva Y, Anselmo D. Multipollutant surface objective analyses and mapping of air
673 quality health index over North America. *Air Qual Atmos Health*. 2016;9(7):743-59. doi:
674 10.1007/s11869-015-0385-9.

675 Pagowski, M., G. A. Grell, S. A. McKeen, S. E. Peckham, and D. Devenyi (2010), Three-dimensional
676 variational data assimilation of ozone and fine particulate matter observations: Some results using the Weather
677 Research and Forecasting–Chemistry model and grid-point statistical interpolation, *Q. J. R. Meteorol. Soc.*, 136,
678 2013–2024, doi:10.1002/qj.700.

679 Pagowski, M., Liu, Z., Grell, G. A., Hu, M., Lin, H.-C., and Schwartz, C. S.: Implementation of aerosol
680 assimilation in Gridpoint Statistical Interpolation (v. 3.2) and WRF-Chem (v. 3.4.1), *Geosci. Model Dev.*, 7,
681 1621–1627, <https://doi.org/10.5194/gmd-7-1621-2014>, 2014.

682 Park, S.-Y., Dash, U. K., Yu, J., Yumimoto, K., Uno, I., and Song, C. H.: Implementation of an ensemble
683 Kalman filter in the Community Multiscale Air Quality model (CMAQ model v5.1) for data assimilation of
684 ground-level PM_{2.5}, *Geosci. Model Dev.*, 15, 2773–2790, <https://doi.org/10.5194/gmd-15-2773-2022>, 2022.

685 Safford, H. D., Paulson, A. K., Steel, Z. L., Young, D. J. N., & Wayman, R. B. (2022). The 2020 California fire
686 season: A year like no other, a return to the past or a harbinger of the future? *Global Ecology and*
687 *Biogeography*, 31(10), 2005–2025. <https://doi.org/10.1111/geb.13498>

688 Sluka Travis. Generic Explicit Diffusion Operator Added to JEDI. JCSDA News Letter. No. 74, Fall 2024.

689 Schwartz C.S., Z. Liu, H.C. Lin, S.A. McKeen. Simultaneous three-dimensional variational assimilation of
690 surface fine particulate matter and MODIS aerosol optical depth. *J. Geophys. Res. Atmos.*, 117 (2012),
691 10.1029/2011jd017383

692 Sun W. , Z. Liu, D. Chen, P. Zhao, M. Chen. Development and application of the WRFDA-Chem
693 three-dimensional variational (3DVAR) system: aiming to improve air quality forecasting and diagnose model
694 deficiencies. *Atmos. Chem. Phys.*, 20 (2020), pp. 9311-9329, 10.5194/acp-20-9311-2020

695 Tang Y., and coauthors, 2023-1-11: *Develop and Evaluate JEDI-Based Regional Aerosol Data Assimilation for*
696 *NOAA UFS-AQM System*. The 103rd AMS Annual Meeting, Denver, Colorado.

697 Trémolet, Y. and Auligné, T.: The Joint Effort for Data Assimilation Integration (JEDI), JCSDA Quarterly
698 Newsletter, 66, 1–5, <https://doi.org/10.25923/RB19-0Q26>, 2020.

699 Vogel, A., Ménard, R., Abu, J., and Chen, J.: Towards a parametric Kalman filter for operational wildfire plume
700 assimilation: Formulation of the forecast step, EGU sphere [preprint],
701 <https://doi.org/10.5194/egusphere-2025-6386>, 2025.

702 Wang. H. and coauthors. 2021-9-13. Assimilation of Aerosol Optical Depth (AOD) retrievals and PM_{2.5} in
703 NCEP’s Next-Generation Regional Air Quality Forecasting System. WCRP-WWRP Symposium on DA and
704 reanalysis. 2021.

705 Wang, H, and coauthors, 2023-5-16: Assimilation of Surface Particulate Matter Observations in the
706 experimental Rapid Refresh Forecast System coupled with Smoke and Dust Model. CU/CIRES Rendezvous
707 2023, Boulder, Colorado.

708 (https://insidecires.colorado.edu/rendezvous/uploads/Rendezvous_2023_7732_1683821981.pdf, last access,
709 July 19 2025)
710 Wang, H, and coauthors, 2025-01-15: Aerosol Data Assimilation within JEDI for the NOAA's Regional Air
711 Quality Model(AQM). The 105th Annual Meeting of the American Meteorological Society, New Orleans, LA.
712 Wei Y., X. Zhao, Z. Zhang, J. Xu, S. Cheng, Z. Liu, W. Sun, X. Chen, Z. Wang, X. Hao, J. Li, D. Chen. Impact
713 of model resolution and its representativeness consistency with observations on operational prediction of PM2.5
714 with 3D-VAR data assimilation. *Atmos. Pollut. Res.*, 15 (2024), Article 102141, 10.1016/j.apr.2024.102141
715 Wang, H., Martin, C., Barré, J., Li, R., Weygandt, S., Huang, J., Tang, Y., Choi, H., Wang, K., Liu, H., & Lee, J.
716 (2025). PM_{2.5} Assimilation within JEDI for NOAA's Regional Air Quality Model (AQMV7): Application to the
717 September 2020 Western U.S. Wildfires [Data set]. Zenodo. <https://doi.org/10.5281/zenodo.17049857>
718 Wen, J., M. Burke. Wildfire smoke plume segmentation using geostationary satellite imagery. arXiv.
719 <https://doi.org/10.48550/arXiv.2109.01637>. 2021.
720 White, Sienna R., R. A. Sugrue, L. Guillotte, E. James, H. Wang, R. Ahmadov, N. Thakur, and F. K. Chow.
721 2026. "Hourly PM2.5 Estimates across California from 2018 to 2023." *ACS ES&T Air*.
722 <https://doi.org/10.1021/acsestair.5c00372>.
723 Zhang, H., Yee, L. D., Lee, B. H., Curtis, M. P., Worton, D. R., Isaacman-VanWertz, G., Offenberg, J. H.,
724 Lewandowski, M., Kleindienst, T. E., Beaver, M. R., Holder, A. L., Lonneman, W. A., Docherty, K. S., Jaoui,
725 M., Pye, H. O. T., Hu, W., Day, D. A., Campuzano-Jost, P., Jimenez, J. L., Guo, H., Weber, R. J., de Gouw, J.,
726 Koss, A. R., Edgerton, E. S., Brune, W., Mohr, C., Lopez-Hilfiker, F. D., Lutz, A., Kreisberg, N. M., Spielman,
727 S. R., Hering, S. V., Wilson, K. R., Thornton, J. A. and Goldstein, A. H.: Monoterpenes are the largest
728 source of summertime organic aerosol in the southeastern United States. *Proc. Natl. Acad. Sci.*, 115,
729 2038-2043, doi.org/10.1073/pnas.1717513115, 2018.